

Terahertz spectroscopy of quantum 2D electron systems

James Lloyd-Hughes

University of Warwick, Department of Physics, Gibbet Hill Road, Coventry, CV4 7AL, UK

E-mail: j.lloyd-hughes@warwick.ac.uk

Received 5 May 2014, revised 17 June 2014

Accepted for publication 23 June 2014

Published 28 August 2014

Abstract

Terahertz time-domain spectroscopy permits the coherent motion of charges to be examined in a diverse range of two-dimensional semiconductor heterostructures. Studies of the THz conductivity and magnetoconductivity of two-dimensional quantum systems are reviewed, including cyclotron resonance spectroscopy and the transverse conductivity in the Hall and quantum Hall regimes. Experiments are described that demonstrate quantum phenomena at THz frequencies, principally coherent control and enhanced light–matter coupling in electromagnetic cavities.

Keywords: terahertz, conductivity, 2D

(Some figures may appear in colour only in the online journal)

1. Introduction

Spectroscopy in the terahertz (THz) frequency range provides an invaluable probe of the electronic properties of materials [1–4]. The last decade has seen an explosion in the development and utilization of terahertz sources and detectors [5], driven in part by the proliferation and uptake of terahertz time-domain spectroscopy (THz-TDS). The meV energy scale (1 THz = 4.14 meV) of THz radiation allows the electronic motion of quasiparticles close to equilibrium to be explored. THz-TDS provides a powerful means to perform broadband, high fidelity and coherent measurements in the far-infrared. Further, optical-pump, THz probe spectroscopy (also termed time-resolved terahertz spectroscopy) uniquely allows the dynamics of transient, non-equilibrium photoexcited charges and excitons to be examined on picosecond to nanosecond timescales [1, 4, 6].

These advances in THz techniques have produced exciting and beautiful physical investigations. In this article THz spectroscopy studies of two-dimensional electron gases (2DEGs) with significant quantum effects are reviewed. Since THz-TDS performs a phase-resolved measurement of an electric field transient it is well suited to probe quantum coherent phenomena. Investigations of (magneto)conductivity, cyclotron resonances, the quantum Hall effect and strong cavity-quasiparticle coupling effects define the main scope of this article. Electrons, excitons

and cavity polaritons are amongst the zoo of quasiparticles that interact with THz radiation, and which are discussed herein. The THz spectroscopy of 2D electronic systems exhibiting quantum confinement is discussed in section 2, including carriers in quantum wells, high mobility 2DEGs, III–V heterostructures and graphene. The influence of a magnetic field on the THz conductivity of these 2D systems is detailed in section 3 in the Hall and quantum Hall regime. Recent studies of cavity polaritons in the strong light–matter coupling regime are highlighted in section 4.

Other recent review articles have provided detailed descriptions of far-field [2] and near-field [7] THz generation and detection; chemical and biological applications [3]; the THz photoconductivity of bulk and nanostructured semiconductors [1, 4, 8, 9]; non-linear THz spectroscopy [10, 11]; metamaterials [12] and anisotropic materials [13–15].

2. Two-dimensional electron systems

2.1. 2D electron gases

Understanding and controlling the conductivity of 2DEGs is vital to the operation of field-effect transistors and quantum well lasers. The frequency-dependent complex conductivity $\sigma(\omega) = \sigma_1 + i\sigma_2$ of a thin charge sheet can be determined exactly from THz-TDS experiments, using analytical expressions given for instance in [4]. To probe the conductivity

of a 2DEG transmission experiments are typically performed at normal incidence, where the electric field of the THz probe is in the plane of the 2D carriers. Here the simple Drude model of free-carrier absorption often describes the THz conductivity, despite being derived for a non-interacting gas of charges, as in-plane motion is not confined. For inhomogeneous systems with lower dimensionality (such as nanoparticles, nanowires, or planar 2D heterostructures in the growth direction) the THz electric field probes a confined electron gas, and alternative conductivity models are needed [1, 4].

Kabir *et al* [16] studied the in-plane conductivity of GaAs and InAs two-dimensional electron gases (2DEGs). They found that the electron scattering time was a function of frequency, indicating that the frequency-dependent conductivity $\sigma(\omega)$ did not obey the Drude model. A generalized $\sigma(\omega)$ model based on the Boltzmann transport equation suggests that this can occur when the chemical potential is large enough for LO-phonon emission to create a scattering rate that depends on the electron energy [17].

Importantly, Kabir *et al* [16] highlighted that the scattering time $\tau_{tr} = 90$ ps from dc transport was substantially greater than the THz scattering time $\tau \sim 200$ fs for a GaAs 2DEG with sheet density $n = 2.3 \times 10^{11} \text{ cm}^{-2}$ at 2 K. THz-TDS measures the ac response of an electron over short distances, while dc transport approaches measure electron motion on macroscopic length scales. The THz scattering time τ was comparable to the quantum scattering time τ_q obtained from Shubnikov de Haas oscillations. The ratio of τ_{tr} to τ_q can be used to investigate the relative importance of large and small angle scattering [16, 18]. Further such comparative studies are required to establish if the THz scattering time and quantum lifetime are universally comparable. Larger THz scattering times were reported for electrons in other III–V 2DEGs at 4 K [19], with $\tau = 1.6$ ps for a three-well terahertz quantum cascade laser design (electron density $N \sim 2 \times 10^{15} \text{ cm}^{-3}$ in the occupied wells) and $\tau = 0.6$ ps for a modulation-doped multiple quantum well ($N \sim 1 \times 10^{17} \text{ cm}^{-3}$ in each quantum well).

2.2. Electrons in heterostructures

Time-domain THz techniques have been used to study 2D semiconductor heterostructures for over two decades. Important early work included the demonstration of Bloch oscillations (oscillatory electron motion in a periodic potential under a static electric field) in semiconductor superlattices using THz radiation emission [20] and an electro-optic sampling method [21, 22]. More recently, the intersubband gain of operating THz quantum cascade lasers was determined using THz-TDS [23], in which the gain was found to be clamped at the absorptive losses of the surface plasmon waveguide when lasing. A laterally integrated Auston switch permitted the gain of a THz-QCL to be unclamped, allowing it to be used as a THz amplifier [24].

2.3. Excitons in quantum well systems

The quantum confinement of electrons and holes in low-dimensional structures can enhance their binding energy, promoting the formation of excitons (bound electron–hole

pairs). In III–V quantum wells (such as GaAs/AlGaAs systems) the exciton binding energies fall in the THz range. The ultrafast formation and decay of excitons in quantum wells was elucidated by Kaindl *et al* [25], who found that excitons formed rapidly upon the resonant photoexcitation of a GaAs multiple quantum well system at low temperature. THz radiation can be strongly absorbed by an exciton, by promoting it from the hydrogenic 1s state into the 2p state, creating a peak in the THz conductivity spectra at finite frequencies (rather than at zero frequency, as for a free electron gas). Subsequent studies identified that at higher exciton densities the system again acts like a free electron–hole plasma, when exciton wavefunctions overlap [26, 27].

2.4. Electrons in graphene

Monolayer graphene exhibits numerous rare and surprising electronic properties, including the infamous Dirac cones near the K -points with linear dispersion, and room-temperature ballistic transport [28, 29]. Above the THz range graphene exhibits a flat optical conductivity $\pi e^2/2h$ characteristic of Dirac fermions, while a Drude-like absorption has been reported in the THz range. The equilibrium and non-equilibrium responses of graphene at THz frequencies are reviewed in detail in [9]. Results may not only depend on sample morphology but on atmospheric environment [30]. The integration of metamaterials with graphene is being explored for plasmonic devices in the THz range [31, 32].

3. THz magnetoconductivity: cyclotron resonance and (quantum) Hall effect

The effective mass of a charge carrier in a semiconductor is a vital property that describes the dispersion of an energy band. Cyclotron resonance spectroscopy has long provided direct experimental insights into the electronic bandstructure of semiconductors, for instance in establishing the ellipsoidal conduction band shape in silicon [33]. Traditionally these measurements were performed with CW far-infrared gas lasers at single (or multiple) frequencies, and sweeping the magnetic field, or with Fourier-transform infrared spectroscopy. THz-TDS provides a valuable alternative technique, offering a broad bandwidth and high signal-to-noise ratio, and with the potential to investigate coherent effects. Experimentally, THz pulses can be generated externally and focussed onto a sample placed in a static or pulsed magnet with optical access. While helium-cooled superconducting dc magnets are often used, pulsed fields with compact nitrogen-cooled solenoids are an alternative [34, 35]. Instead of free-space external optics, THz pulses can be generated and detected inside the bores of magnets without windows using fibre-coupled THz antennae [36].

Perpendicular magnetic and electric fields applied to a semiconductor are well known to create phenomena such as the Hall effect and quantum Hall effect (QHE). For a THz electric field applied in the x direction and an external magnetic field in the z direction the x – y plane THz conductivity is described

as a tensor $\sigma_{ij}(\omega)$. In the case of the Drude–Lorentz model the frequency-dependent conductivity tensor is [37]

$$\sigma_{ij}(\omega) = \frac{\sigma_0}{(1 - i\omega\tau)^2 + \omega_c^2\tau^2} \begin{pmatrix} 1 - i\omega\tau & \omega_c\tau \\ -\omega_c\tau & 1 - i\omega\tau \end{pmatrix} \quad (1)$$

in the plane perpendicular to B , where $\omega_c = eB/m^*$ is the cyclotron frequency. The on-diagonal components are equal for all magnetic fields when the material is isotropic in the x – y plane, i.e. $\sigma_{xx} = \sigma_{yy}$. The off-diagonal terms σ_{xy} , σ_{yx} describe the conductive response orthogonal to the applied electric field, as an ac analogue to the traditional dc Hall effect. Since the off-diagonal component of the optical response is non-zero, and varies with B , a 2DEG under a magnetic field exhibits the magneto-optic effect whereby the polarization state of incident light is altered and depends on B . Indeed, ellipsometric studies using THz-TDS (discussed below and in [14]) have examined magnetic-field induced rotations of the polarization state of THz radiation in the transmission (Faraday) and reflection (Kerr) geometries.

Before reviewing recent experimental studies of the magnetoconductivity at THz frequencies in 2DEGs and graphene, pertinent background information regarding the effective mass and cyclotron resonance is given.

3.1. Background: effective mass

Anisotropy in the valence and/or conduction band requires a tensor definition of the effective mass m_{ij}^* , which is often given by the relation

$$\frac{1}{m_{ij}^*} = \frac{1}{\hbar^2} \frac{d^2 E}{dk_i dk_j}. \quad (2)$$

This expression is valid, however, only for *parabolic* energy dispersion relations of the form $E(k) = \hbar^2 k^2 / 2m^*$. This is the case for group III–V or group IV semiconductors when the chemical potential is not high in the conduction band or low in the valence band—i.e. in the low density limit. The effective mass by this definition is a constant specific to the electronic bandstructure, and is independent of material properties such as the electron density or external parameters such as a magnetic field. A general definition of the effective mass for *arbitrary* energy dispersion relations can be derived by considering an electron as a wavepacket [38]. This approach yields

$$m^* = \frac{p}{dE/dp}, \quad (3)$$

for an electron with crystal momentum $p = \hbar k$. For materials with a linear energy dispersion relation such as graphene, which has $E = v_F p$ for Fermi velocity v_F , this predicts that the effective mass increases linearly with electron momentum according to $m^* = p/v_F = E/v_F^2$ [29, 38]. The same equation (3) can also be used to account for the energy-dependent effective mass of semiconductors when the conduction band cannot be regarded as purely parabolic [38].

3.2. Background: cyclotron resonance

Classically, under the influence of a magnetic field B charges move in circular orbits with angular frequency $\omega_c = eB/m^*$.

Quantum mechanically, the application of a magnetic field in the z -direction quantizes the cyclotron orbits in the x – y plane [39], with an extra energy given by

$$E_{n,\sigma}(B) = \left(n + \frac{1}{2}\right) \hbar\omega_c + \sigma g^* \mu_B B, \quad (4)$$

where $n = 0, 1, 2 \dots$ denotes the Landau level index, and electrons have effective mass m^* , g -factor g^* and spin $\sigma = \pm 1/2$. This expression is valid for 3D semiconductors and also for ‘quasi’-2D materials such as III–V or II–VI quantum wells, if subband structure is ignored (valid when quantum confinement acts in the z -direction). In monolayer graphene, Landau level energies are instead given by [29]

$$E_{\pm n}(B) = v_F \sqrt{2e\hbar B n}, \quad (5)$$

for integer $n \geq 0$.

Electric-dipole allowed transitions between Landau levels are permitted when the level index changes by $\Delta n = \pm 1$. If spin–orbit coupling is weak, then only Landau levels with the same spin state are coupled (i.e. $\Delta\sigma = 0$), and the Zeeman term (the second term in equation (4)) does not contribute to the allowed transitions, which have energy $E_{n+1} - E_n = \hbar\omega_c$. Thus electrons in Landau levels can emit or absorb electromagnetic radiation with an energy $\hbar\omega_c = eB/m^*$. Even when spin–orbit coupling is present the Zeeman term may still be disregarded for small magnetic fields ($B < 5$ T), as it is smaller than typical Landau level widths.

In order for a cyclotron resonance to be experimentally observable, the time period of one cyclotron orbit must be substantially shorter than the mean time τ between carrier scattering events. This places the restriction that $\omega_c \gg 2\pi/\tau$. Thus for materials with short carrier scattering lifetime (low mobility) $\tau < 1$ ps cyclotron resonances can only be observed at high frequencies, in the THz range.

The density of states of Landau levels [39] is shown schematically in figure 1(a) in the classical limit, where Landau levels overlap at low B or high widths Γ (in energy). For small Γ or higher B discrete Landau levels are formed, and the system can be regarded as a two-level quantum system. This is pictured in figure 1(b) assuming degenerate spin states.

3.3. Bulk semiconductors

For semiconductors with parabolic but anisotropic bands, such as silicon and germanium, multiple electron cyclotron resonances can be observed, with frequencies that vary with crystallographic orientation with respect to the applied magnetic field [33]. Holes generally have large effective masses, and are therefore harder to examine experimentally as the magnetic fields required are larger. THz-TDS in conjunction with a pulsed magnet was used to determine the light and heavy hole masses in p-type Ge oriented such that $B // [110]$ [34].

The on-diagonal and off-diagonal (Hall) components of the magnetoconductivity tensor were determined by Mittleman *et al* [37], who performed polarization-resolved THz-TDS transmission studies of a 1 μ m thick doped GaAs sample

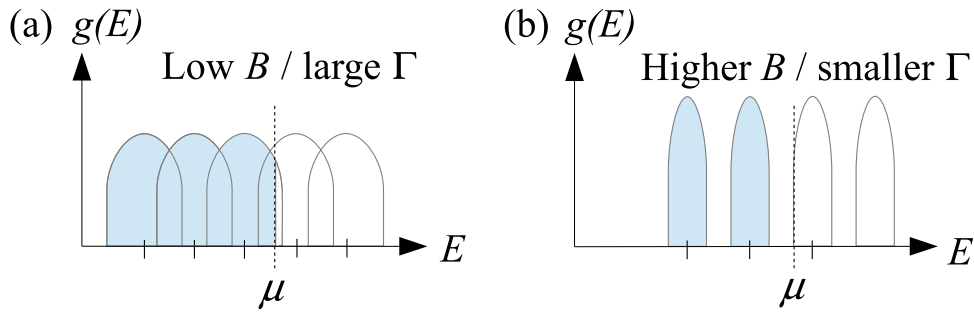


Figure 1. Density of states $g(E)$ versus energy E in a magnetic field B for chemical potential μ . (a) Classical limit, where Landau levels overlap at low B , or high linewidth Γ . (b) Quantum limit, when B is large enough (or Γ small enough) that discrete Landau levels emerge.

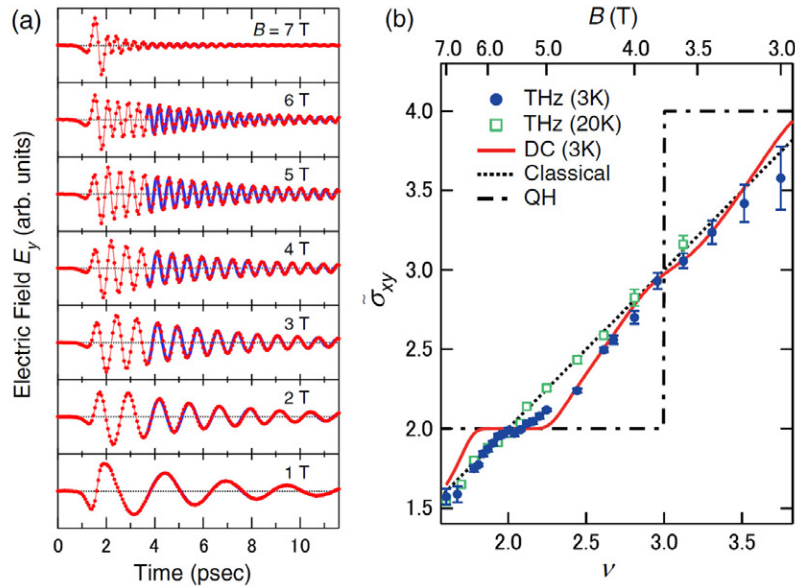


Figure 2. Quantum Hall effect at THz frequencies. (a) THz electric field E_y , orthogonal to the incident pulse E_x at various magnetic fields and at 3 K. (b) Normalized σ_{xy} from THz-TDS versus Landau level filling fraction ν at 3 K, showing a plateau-like feature consistent with the integer quantum Hall effect at $\nu = 2$, which disappears at 20 K. Reproduced with permission from [45], Copyright 2010 American Physical Society.

at room temperature. Raster scans were used to create images of the carrier density and mobility across the sample. Crossed wire-grid polarizers were used by Ikebe and Shimano [40] to determine the Faraday rotation of THz radiation transmitted through lightly-doped silicon, in magnetic fields as low as $B = 0.01$ T, and as a function of temperature. A similar approach was used by Yatsugi *et al* [41], who instead performed reflection (Kerr) geometry studies of n-type InAs wafers. By examining a variety of samples with different doping densities, the effective mass was found to increase with electron density as a consequence of non-parabolicity in the conduction band. These studies demonstrate the technological importance of THz-TDS in characterizing the conductivity of semiconductor wafers in a non-contact fashion.

3.4. Quantum wells and heterostructures

The electron cyclotron resonance of a single GaAs/AlGaAs heterojunction was examined using THz-TDS to reveal the cyclotron response (from σ_{xx}) in the time-domain [42]. A semi-transparent gate electrode was used to modulate

the electron density in the 2DEG, allowing the scattering time ($\tau \sim 3$ ps at 4 K) to be studied as a function of chemical potential and temperature. As an alternative to gate modulation, a comparison of the THz transmission at B and zero magnetic field yields the magnetic-field induced change in conductivity. Using this approach higher mobility GaAs 2DEGs with $\tau = 16$ ps were studied [43]. The electron cyclotron resonance, and the splitting of the THz excitonic 1s-2p transition under a magnetic field, have also been examined in GaAs/AlGaAs THz quantum cascade structures [44].

In the quantum Hall regime the off-diagonal conductivity σ_{xy} is quantized, as a consequence of the large spacing between Landau levels [39]. In analogy to the static QHE at $\omega = 0$, the dynamic (or optical) QHE has been discovered using THz-TDS [45]. In these experiments, the electric field response orthogonal (E_y) and parallel (E_x) to the incident THz pulse was recorded for a GaAs 2DEG. The lifetime $\tau = 6$ ps can be seen from the decay of E_y in figure 2(a). The transverse THz magnetoconductivity $\tilde{\sigma}_{xy}$ shown in figure 2(b) exhibits a clear plateau around integer Landau level filling index $\nu = 2$ at 3 K (circles), demonstrating that the dynamic ac conductive

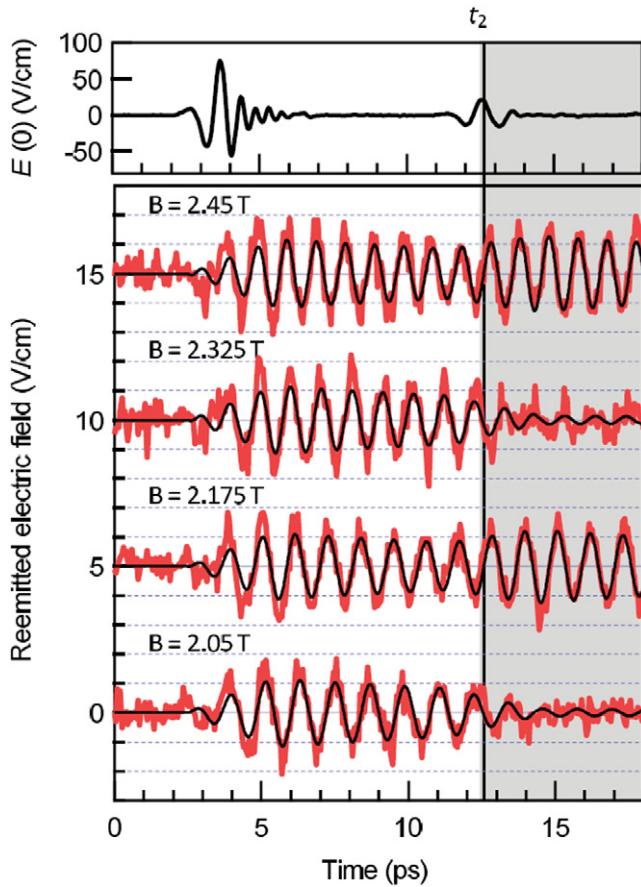


Figure 3. Coherent control of cyclotron oscillations in a GaAs 2DEG at 1.4 K. Top panel: incident THz pulses E_x . Bottom panel: THz pulse in E_y direction at various magnetic fields. Depending on B the oscillation induced by the second pulse interferes constructively or destructively with that from the first pulse. Reproduced with permission from [48], Copyright 2011 American Physical Society.

response is also quantized. In this figure, $\tilde{\sigma}_{xy}$ is the off-diagonal conductivity with the cyclotron line's contribution divided out, in units of e^2/h , and averaged over 2–5 meV. The system returns to classical (Drude–Lorentz magnetoconductivity) behaviour at elevated temperatures (20 K, squares). The THz QHE was also investigated in strained HgTe quantum wells by Shuvaev *et al* [46], a system of interest as a 3D topological insulator.

Excitation schemes using multiple THz pulses have been used to examine coherent cyclotron oscillations directly in the time domain. Huggard *et al* [47] used photoconductive emitters photoexcited with two IR pulses with variable time delay to drive cyclotron oscillations in a GaAs 2DEG. When the time spacing between the two pulses was an even integer multiple of the cyclotron period the time-domain THz cyclotron oscillation was constructively enhanced, while for odd integer multiples destructive interference occurred. Similar results were obtained by Arikawa *et al* [48] using two THz pulses with a fixed time delay, and by tuning the magnetic field, as illustrated in figure 3. At $B = 2.05, 2.325$ T the second THz pulse is in anti-phase, and destructive interference of the cyclotron oscillation occurs, while at $B = 2.175, 2.45$ T constructive interference occurs and the oscillation is

enhanced. A model based on the optical Bloch equations for a two-level quantum system (black lines) reproduces the experimental oscillations (red lines).

3.5. Graphene

In contrast to the standard quantum Hall effect, graphene exhibits a half-integer QHE whereby the Hall conductivity is $\sigma_{xy} = \pm 4(n + 1/2)e^2/h$ for integer Landau level index n [28]. The half-integer shift in comparison to the standard QHE arises from a Landau level at the K -point ($E = 0$ for $n = 0$ in equation (5)), shared by electrons and holes, while the factor of 4 results from double spin and double valley degeneracy. Cyclotron resonance studies on graphene devices have demonstrated that $E_N \propto \sqrt{B}$, and $m^* \propto \sqrt{N}$ for carrier density N [49, 50], consistent with a linear dispersion at the Fermi level. The magneto-optics of intraband and interband Landau level transitions are detailed for graphene and related allotropes of carbon in Orlita and Potemski's review article [51].

Recently Shimano *et al* [52] investigated the THz quantum Hall effect in epitaxial graphene on SiC. The Faraday rotation angle θ_F was determined by THz-TDS in the range 2–10 meV and at 5 K, in the geometry depicted in figure 4(a). At low magnetic fields the frequency-dependence of θ_F (points in figure 4(b)) was well modelled by the Drude–Lorentz formalism (lines). For $B \geq 1$ T the Faraday angle was frequency independent (figure 4(c)), and did not change in magnitude for $B \geq 4$ T. In figure 4(d) the Faraday angle at 1 THz is reported versus B (points), indicating the two magnetic field regimes. At low fields $|\theta_F| \propto B$, as expected for the linear Faraday effect. Plateau-like deviations from the Drude model's prediction (dashed line, based on E_F and τ), are clear above $B = 3$ T, and are a direct consequence of the system entering the quantum Hall regime. Two forms of theoretical calculation for the ac Hall effect are shown by the solid and dotted lines, highlighting plateaux at $\nu = 2, 6$.

4. Strong light–matter coupling in cavities

The light–matter interaction can be dramatically enhanced in cavities that confine electromagnetic modes into small volumes. The interaction between atomic-like quantum systems and quantized electromagnetic radiation is of great interest in quantum optics, and can be treated theoretically by the Jaynes–Cummings model for a two-level atom interacting with a single cavity mode [53]. In condensed matter systems cavity polaritons result with altered dispersion relations: rather than a 'bare' interaction at energy $\hbar\omega_0$, in a cavity two energy eigenstates emerge centred around $\hbar\omega_0$ and split by the vacuum Rabi energy $2\hbar\Omega$. The figure of merit Ω/ω_0 describing the strength can be extremely large in the terahertz range, with Rabi frequencies comparable to the resonance frequency. This has motivated a number of recent investigations to explore this ultra-strong limit, where energy exchange occurs on timescales similar to the period of the electromagnetic radiation, and non-perturbative theories are required.

Intersubband cavity polaritons were examined in the THz frequency range by Todorov *et al* [54], who used

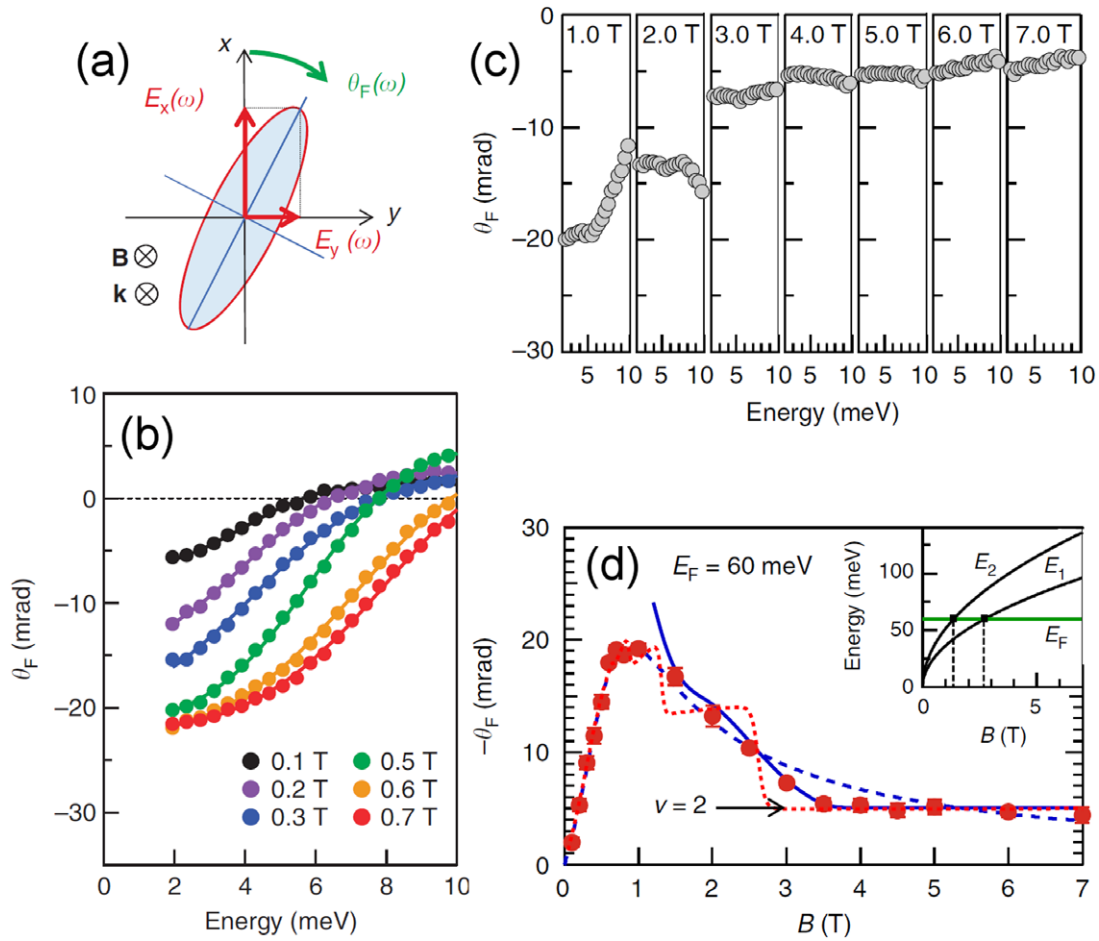


Figure 4. THz quantum Hall effect in epitaxial graphene. (a) Experimental geometry. (b) and (c) Faraday rotation angle θ_F at low and high magnetic fields B , respectively. (d) $\theta_F(B)$ from experiment (points), the classical Drude–Lorentz model (dashed line), and two optical Hall effect calculations (solid and dotted lines). The inset shows the Landau levels. Reproduced with permission from [52], Copyright 2013 Nature.

FTIR transmission and reflection spectroscopy to characterize 32 nm-wide GaAs quantum wells with an intersubband frequency $\omega_0/2\pi = 3.6$ THz between the ground state $|0\rangle$ and first excited state $|1\rangle$. The wells were Si-doped, with the chemical potential inbetween $|0\rangle$ and $|1\rangle$ such that only the ground state was populated at low temperatures. Multi-pass transmission measurements on a sample completely top-coated with metal (figure 5(a)) established that the bare intersubband transition is visible below 60 K. When a metal-dielectric cavity is introduced with a mode at the same frequency, a splitting of the intersubband line into two is evident in the reflectivity at low temperature, as shown in figure 5(b). A ratio $\Omega/\omega_0 = 0.22$ was observed by evaluating splittings for various cavities with different frequency detunings.

The controlled photoinjection of electrons into GaAs QWs (in a mid-IR waveguide) using a 12 fs IR pump pulse has enabled the formation of cavity polaritons in the mid-IR range to be directly resolved in the time-domain [55]. An enhanced cavity polariton splitting with fluence was observed, and the time-scale for cavity polariton formation was around 100 fs.

As an alternative to square quantum wells, cavity intersubband polaritons in parabolic quantum wells have been investigated by Geiser *et al* [56,57]. In parabolic

wells the energy spacing between eigenstates is constant, and therefore high temperatures do not degrade intersubband absorption (unlike the case in square quantum wells). Room temperature intersubband cavity polaritons were observed with $\Omega/\omega_0 = 0.14$, utilizing cavities comprising two circular capacitor elements linked with a narrow wire-like inductive element. Changing the length of the bridge altered the inductance, tuning the cavity resonance across the intersubband energy. Electroluminescence from THz cavity intersubband polaritons at room temperature [58] and gate-voltage tuned frequencies [59] have also been reported. These findings highlight important potential applications for strong-coupling effects at room temperature.

A 2DEG in a strong magnetic field B can be modelled as a two-level system, as discussed in section 3. Scalfari *et al* [60] demonstrated a strong coupling between the cyclotron resonance and the resonances of metamaterials consisting of split ring resonators. One advantage of this approach is that the two-level system’s resonance frequency can be directly tuned across different cavity modes by altering B . In figure 6 the transmission from THz-TDS of a metamaterial containing an array of split ring resonators (one pictured in the inset) is shown against B . Rather than just the electron cyclotron

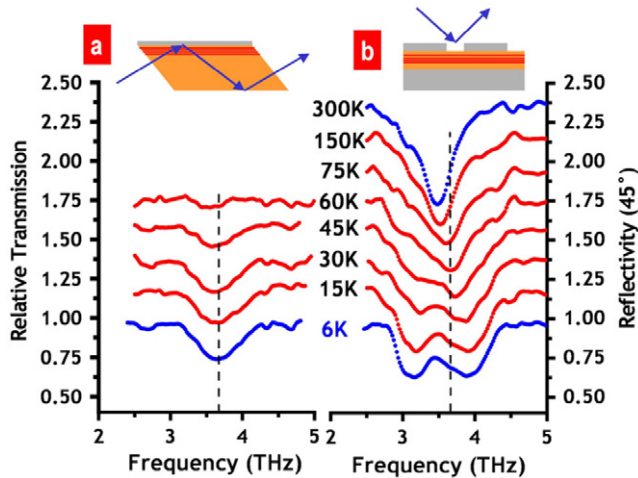


Figure 5. THz intersubband cavity polaritons in the strong coupling regime. (a) Transmission measurements showing the bare intersubband absorption at 3.6 THz. (b) Reflectivity measurements on cavity-coupled intersubband polaritons exhibiting mode splitting. Reproduced with permission from [54], Copyright 2009 American Physical Society.

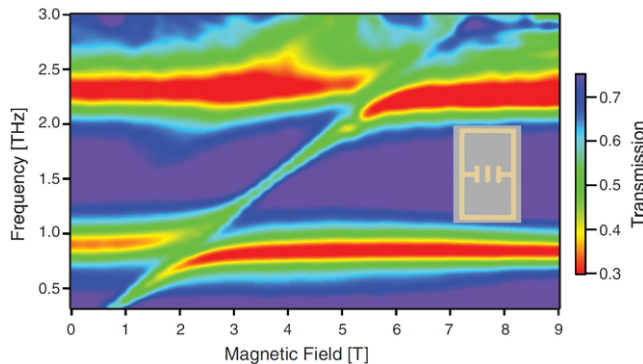


Figure 6. Strong coupling between the THz cyclotron resonance and the resonances of a split ring resonator array. The THz absorption is dramatically different from the single straight line case expected for the cyclotron resonance. Upper and lower magnetopolariton branches are visible for both 0.9 THz and 2.3 THz cavity modes. The inset shows the split-ring resonator, which was repeated across the sample's surface. Reproduced with permission from [60], Copyright 2012 AAAS.

resonance, upper and lower magnetopolariton branches are clear around the two lowest frequency modes (at 0.9 THz and 2.3 THz) of the resonator. $\Omega/\omega_0 = 0.17$ was obtained for the lowest resonance. By tailoring the electron density with multiple 2DEGs, and adopting an alternative resonator design, enhanced coupling $\Omega/\omega_0 = 0.58$ was obtained [60]. Variations on metamaterial design [61] and the use of superconducting split-ring resonators [62] have been explored recently.

5. Conclusion and outlook

Terahertz spectroscopy and time-domain THz techniques have emerged as invaluable for disparate areas of physics, including 2D electronic systems. Not only can the fundamental properties of novel conductive materials and artificial materials

be explored with unprecedented detail, new experimental paradigms in quantum optics and quantum coherence can now be leveraged. The coming decade will continue to see the growth and adaptation of THz technology, and will hopefully lead to exciting new discoveries. The application of the methodologies discussed herein to novel materials such as graphene-like 2D semiconductors and semimetals, oxide based 2DEGs and topological insulators will provide fertile ground for future research on novel states of matter. Dynamic analogues of new physical phenomena, such as the fractional quantum Hall effect, may be explored. Recent dramatic improvements in THz-TDS with high electric fields (above MV/cm) will permit investigations of the non-linear response of carriers, allowing quantum kinetic theories to be tested.

Acknowledgments

The author would like to acknowledge the EPSRC (UK) for a Fellowship, grant EP/H003444/2.

References

- [1] Ulbricht R, Hendry E, Shan J, Heinz T F and Bonn M 2011 Carrier dynamics in semiconductors studied with time-resolved terahertz spectroscopy *Rev. Mod. Phys.* **83** 543–86
- [2] Jepsen P U, Cooke D G and Koch M 2011 Terahertz spectroscopy, imaging—modern techniques, applications *Laser Photon. Rev.* **5** 124–66
- [3] Baxter J B and Guglietta G W 2011 Terahertz spectroscopy *Anal. Chem.* **83** 4342–68
- [4] Lloyd-Hughes J and Jeon T-I 2012 A review of the terahertz conductivity of bulk and nano-materials *J. Infrared, Millimeter, Terahertz Waves* **33** 871
- [5] Tonouchi M 2007 Cutting-edge terahertz technology *Nature Photon.* **1** 97–105
- [6] Schmuttenmaer C A 2004 Exploring dynamics in the far-infrared with terahertz spectroscopy *Chem. Rev.* **104** 1759–79
- [7] Adam A J L 2011 Review of near-field terahertz measurement methods and their applications *J. Infrared, Millimeter, Terahertz Waves* **32** 1
- [8] Němec H, Kužel P and Sundström V 2010 Charge transport in nanostructured materials for solar energy conversion studied by time-resolved terahertz spectroscopy *J. Photochem. Photobiol. A* **215** 123–39
- [9] Docherty C J and Johnston M B 2012 Terahertz properties of graphene *J. Infrared, Millimeter, Terahertz Waves* **33** 797
- [10] Kampfrath T, Tanaka K and Nelson K A 2013 Resonant and nonresonant control over matter and light by intense terahertz transients *Nature Photon.* **7** 680–90
- [11] Woerner M, Kuehn W, Bowlan P, Reimann K and Elsaesser T 2013 Ultrafast two-dimensional terahertz spectroscopy of elementary excitations in solids *New J. Phys.* **15** 025039
- [12] Keiser G R, Fan K, Zhang X and Averitt R D 2013 Towards dynamic, tunable, and nonlinear metamaterials via near field interactions: a review *J. Infrared, Millimeter, Terahertz Waves* **34** 709–23
- [13] Nagashima T, Tani M and Hangyo M 2013 Polarization-sensitive THz-TDS and its application to anisotropy sensing *J. Infrared, Millimeter, Terahertz Waves* **34** 740–75
- [14] Arikawa T, Zhang Q, Ren L, Belyanin A A and Kono J 2013 Review of anisotropic terahertz material response *J. Infrared, Millimeter, Terahertz Waves* **34** 724–39

- [15] Wiesauer K and Jördens C 2013 Recent advances in birefringence studies at THz frequencies *J. Infrared, Millimeter, Terahertz Waves* **34** 663–81
- [16] Kabir N A, Yoon Y, Knab J R, Chen J Y, Markelz A G, Reno J L, Sadofyev Y, Johnson S, Zhang Y H and Bird J P 2006 Terahertz transmission characteristics of high-mobility GaAs and InAs two-dimensional-electron-gas systems *Appl. Phys. Lett.* **89** 132109
- [17] Lloyd-Hughes J 2012 Generalized conductivity model for polar semiconductors at terahertz frequencies *Appl. Phys. Lett.* **100** 122103
- [18] Coleridge P 1991 Small-angle scattering in two-dimensional electron gases *Phys. Rev. B* **44** 3793–801
- [19] Lloyd-Hughes J, Delley Y L, Scalari G, Fischer M, Liverini V, Beck M and Faist J 2009 Spectroscopic determination of the doping and mobility of terahertz quantum cascade structures *J. Appl. Phys.* **106** 093104
- [20] Waschke C, Roskos H, Schwedler R, Leo K, Kurz H and Köhler K 1993 Coherent submillimeter-wave emission from Bloch oscillations in a semiconductor superlattice *Phys. Rev. Lett.* **70** 3319–22
- [21] Dekorsy T, Leisching P, Köhler K and Kurz H 1994 Electro-optic detection of Bloch oscillations *Phys. Rev. B* **50** 8106–9
- [22] Dekorsy T, Ott R, Kurz H and Köhler K 1995 Bloch oscillations at room temperature *Phys. Rev. B* **51** 17275–8
- [23] Kröll J, Darmo J, Dhillon S S, Marcadet X, Calligaro M, Sirtori C and Unterrainer K 2007 Phase-resolved measurements of stimulated emission in a laser *Nature* **449** 698
- [24] Jukam N, Dhillon S S, Oustinov D, Madeo J, Manquest C, Barbieri S, Sirtori C, Khanna S P, Linfield E H, Davies A G and Tignon J 2009 Terahertz amplifier based on gain switching in a quantum cascade laser *Nature Photon.* **3** 715–9
- [25] Kaindl R A, Carnahan M A, Hägele D, Lövenich R and Chemla D S 2003 Ultrafast terahertz probes of transient conducting, insulating phases in an electron-hole gas *Nature* **423** 734–8
- [26] Huber R, Kaindl R A, Schmid B A and Chemla D S 2005 Broadband terahertz study of excitonic resonances in the high-density regime in GaAs/Al_xGa_{1-x}As quantum wells *Phys. Rev. B* **72** 161314
- [27] Kaindl R A, Hägele D, Carnahan M A and Chemla D S 2009 Transient terahertz spectroscopy of excitons and unbound carriers in quasi-two-dimensional electron-hole gases *Phys. Rev. B* **79** 045320
- [28] Geim A K and Novoselov K S 2007 The rise of graphene *Nature Mater.* **6** 183–91
- [29] Neto A H C, Guinea F, Peres N M R, Novoselov K S and Geim A K 2009 The electronic properties of graphene *Rev. Mod. Phys.* **81** 109–62
- [30] Docherty C J, Lin C, Joyce H J, Nicholas R J, Herz L M, Li L and Johnston M B 2012 Extreme sensitivity of graphene photoconductivity to environmental gases *Nature Commun.* **3** 1228
- [31] Valmorra F, Scalari G, Maissen C, Fu W, Schönenberger C, Choi J W, Park H G, Beck M and Faist J 2013 Low-bias active control of terahertz waves by coupling large-area CVD graphene to a terahertz metamaterial *Nano Lett.* **13** 3193–8
- [32] Otsuji T, Popov V and Ryzhii V 2014 Active graphene plasmonics for terahertz device applications *J. Phys. D: Appl. Phys.* **47** 094006
- [33] Dresselhaus G, Kip A and Kittel C 1955 Cyclotron Resonance of electrons and holes in silicon and germanium crystals *Phys. Rev.* **98** 368–84
- [34] Molter D, Ellrich F, Weinland T, George S, Goiran M, Keilmann F, Beigang R and Léotin J 2010 High-speed terahertz time-domain spectroscopy of cyclotron resonance in pulsed magnetic field *Opt. Express* **18** 26163–8
- [35] Molter D, Torosyan G, Ballon G, Drigo L, Beigang R and Léotin J 2012 Step-scan time-domain terahertz magneto-spectroscopy *Opt. Express* **20** 5993–6002
- [36] Crooker S A 2002 Fiber-coupled antennas for ultrafast coherent terahertz spectroscopy in low temperatures and high magnetic fields *Rev. Sci. Instrum.* **73** 3258
- [37] Mittleman D M, Cunningham J, Nuss M C and Geva M 1997 Noncontact semiconductor wafer characterization with the terahertz hall effect *Appl. Phys. Lett.* **71** 16
- [38] Ariel V 2012 Effective mass and energy–mass relationship arXiv:1205.3995
- [39] Ando T, Fowler A B and Stern F 1982 Electronic-properties of two-dimensional systems *Rev. Mod. Phys.* **54** 437–672
- [40] Ikebe Y and Shimano R 2008 Characterization of doped silicon in low carrier density region by terahertz frequency Faraday effect *Appl. Phys. Lett.* **92** 012111
- [41] Yatsugi K, Matsumoto N, Nagashima T and Hangyo M 2011 Transport properties of free carriers in semiconductors studied by terahertz time-domain magneto-optical ellipsometry *Appl. Phys. Lett.* **98** 212108
- [42] Some D and Nurmikko A V 1994 Real-time electron cyclotron oscillations observed by terahertz techniques *Appl. Phys. Lett.* **65** 3377–79
- [43] Wang X F, Hilton D J, Ren L, Mittleman D M, Kono J and Reno J L 2007 Terahertz time-domain magnetospectroscopy of a high-mobility two-dimensional electron gas *Opt. Lett.* **32** 1845
- [44] Lloyd-Hughes J, Beere H E, Ritchie D A and Johnston M B 2008 Terahertz magnetoconductivity of excitons and electrons in quantum cascade structures *Phys. Rev. B* **77** 125322
- [45] Ikebe Y, Morimoto T, Masutomi R, Okamoto T, Aoki H and Shimano R 2010 Optical Hall effect in the integer quantum Hall regime *Phys. Rev. Lett.* **104** 256802
- [46] Shuvaev A, Astakhov G, Tkachov G, Brüne C, Buhmann H, Molenkamp L and Pimenov A 2013 Terahertz quantum Hall effect of Dirac fermions in a topological insulator *Phys. Rev. B* **87** 121104
- [47] Huggard P G, Cluff J A, Shaw C J, Andrews S R, Linfield E H and Ritchie D A 1997 Coherent control of cyclotron emission from a semiconductor using sub-picosecond electric field transients *Appl. Phys. Lett.* **71** 2647–9
- [48] Arikawa T, Wang X, Hilton D J, Reno J L, Pan W and Kono J 2011 Quantum control of a Landau-quantized two-dimensional electron gas in a GaAs quantum well using coherent terahertz pulses *Phys. Rev. B* **84** 241307
- [49] Novoselov K S, Geim A K, Morozov S V, Jiang D, Katsnelson M I, Grigorieva I V, Dubonos S V and Firsov A A 2005 Two-dimensional gas of massless Dirac fermions in graphene *Nature* **438** 197–200
- [50] Deacon R S, Chuang K C, Nicholas R J, Novoselov K S and Geim A K 2007 Cyclotron resonance study of the electron and hole velocity in graphene monolayers *Phys. Rev. B* **76** 081406
- [51] Orlita M and Potemski M 2010 Dirac electronic states in graphene systems: optical spectroscopy studies *Semicond. Sci. Technol.* **25** 063001
- [52] Shimano R, Yumoto G, Yoo J Y, Matsunaga R, Tanabe S, Hibino H, Morimoto T and Aoki H 2013 Quantum Faraday, Kerr rotations in graphene *Nature Commun.* **4** 1841
- [53] Jaynes E T and Cummings F W 1963 Comparison of quantum and semiclassical radiation theories with application to the beam maser *Proc. IEEE* **51** 89–109
- [54] Todorov Y, Andrews A M, Sagnes I, Colombelli R, Klang P, Strasser G and Sirtori C 2009 Strong light–matter coupling

- in subwavelength metal-dielectric microcavities at terahertz frequencies *Phys. Rev. Lett.* **102** 186402
- [55] Günter G, Anappara A A, Hees J, Sell A, Biasiol G, Sorba L, De Liberato S, Ciuti C, Tredicucci A, Leitenstorfer A and Huber R 2009 Sub-cycle switch-on of ultrastrong light-matter interaction *Nature* **458** 178–81
- [56] Geiser M, Walther C, Scalari G, Beck M, Fischer M, Nevou L and Faist J 2010 Strong light-matter coupling at terahertz frequencies at room temperature in electronic LC resonators *Appl. Phys. Lett.* **97** 191107
- [57] Geiser M, Castellano F, Scalari G, Beck M, Nevou L and Faist J 2012 Ultrastrong coupling regime and plasmon polaritons in parabolic semiconductor quantum wells *Phys. Rev. Lett.* **108** 106402
- [58] Geiser M, Scalari G, Castellano F, Beck M and Faist J 2012 Room temperature terahertz polariton emitter *Appl. Phys. Lett.* **101** 141118
- [59] Geiser M, Beck M and Faist J 2014 Terahertz intersubband polariton tuning by electrical gating *Opt. Express* **22** 2126–31
- [60] Scalari G, Maissen C, Turčinková D, Hagenmuller D, de Liberato S, Ciuti C, Reichl C, Schuh D, Wegscheider W, Beck M and Faist J 2012 Ultrastrong coupling of the cyclotron transition of a 2d electron gas to a THz metamaterial *Science* **335** 1323–6
- [61] Scalari G, Maissen C, Hagenmuller D, De Liberato S, Ciuti C, Reichl C, Wegscheider W, Schuh D, Beck M and Faist J 2013 Ultrastrong light-matter coupling at terahertz frequencies with split ring resonators and inter-Landau level transitions *J. Appl. Phys.* **113** 136510
- [62] Scalari G, Maissen C, Cibella S, Leoni R, Carelli P, Valmorra F, Beck M and Faist J 2014 Superconducting complementary metasurfaces for THz ultrastrong Light-matter coupling *New J. Phys.* **16** 033005